Multiedge refinement of extended x-ray-absorption fine structure of manganese zinc ferrite nanoparticles

S. Calvin,* E. E. Carpenter, B. Ravel, and V. G. Harris
U.S. Naval Research Laboratory, Washington, D.C. 20375

S. A. Morrison
George Washington University, Washington, D.C. 20052
(Received 12 July 2002; published 6 December 2002)

The structure of nanoparticle manganese zinc ferrites synthesized by a reverse micellar method is determined by analysis of the extended x-ray-absorption fine structure in combination with other techniques. Both empirical and theoretical standards are employed; manganese, zinc, and iron edges are refined simultaneously. It is determined that samples synthesized under similar conditions sometimes exhibit a markedly different distribution of cations between the available sites in the spinel structure; this in turn causes significant differences in the magnetic properties of the samples. In addition, it is found that the mean-square displacements for manganese-oxygen bonds are consistently higher than for zinc-oxygen bonds, perhaps due to the presence of manganese ions of more than one valence.

DOI: 10.1103/PhysRevB.66.224405 PACS number(s): 75.75.+a, 61.46.+w, 61.10.Ht

I. INTRODUCTION

For many decades, ferrites have been important magnetic materials for high-frequency industrial applications, due to low conductive losses, high permeabilities, and moderately high saturation magnetizations.[1] These attractive properties, in turn, depend critically on both the magnetic moment of the metal cations and on their distribution between sites with tetrahedral oxygen coordination and those with octahedral coordination. In particular, manganese zinc ferrites (MZFO's) have emerged as the leading materials for inductor applications in the MHz *f* band. In recent years, there has been considerable interest in nanoparticle ferrites, since in many cases they have been found to have technologically desirable magnetic properties relative to ferrites synthesized by traditional routes.[2,3] Some of these properties, such as low coercivity, are attributable directly to the small size of the particles, but others, such as a relatively high Curie temperature, appear to be related to the distribution of cations between sites.[4–8] It is thus important to develop techniques that can identify the cation distribution in these materials.

Because of the similar scattering strengths of manganese, zinc, and iron, it is difficult to rely on x-ray diffraction (XRD) to determine the site occupancy in MZFO's. This problem is exacerbated in nanoparticles, since the loss of long-range order broadens the diffraction peaks, making full profile reduction considerably more difficult. Mössbauer-effect measurements are effective in determining the symmetry and valence of the iron cations, but provide no direct information on the manganese and zinc cations. For these reasons, extended x-ray-absorption fine-structure (EXAFS) spectroscopy has been used to determine site occupancy in nanoparticle MZFO's. Until now, these determinations have examined the manganese, zinc, and iron edges separately, and, although they have been successful in qualitative comparisons (e.g., comparing samples synthesized by different methods), they have generally yielded only limited quantitative information (see Sec. II B). In this work, we describe a method of analyzing the information from the manganese, zinc, and iron edges simultaneously, along with stoichiometric information from inductively coupled plasma (ICP) optical emission spectroscopy, to yield a more precise determination of the site occupancy as well as additional important structural information.

II. BACKGROUND

A. Spinel structure

MZFO adopts the spinel structure, illustrated in Fig. 1. The oxygens in this structure are based on a face-centered-cubic (fcc) lattice. One out of eight of the tetrahedral interstices (*A* sites) and half of the octahedral interstices (*B* sites) are occupied by cations, yielding a total of thirty two oxygens, eight tetrahedrally coordinated cations, and sixteen octahedrally coordinated cations per unit cell. Charge conser-

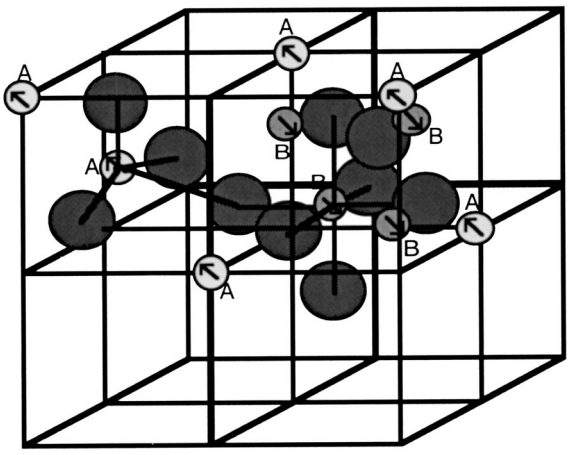

FIG. 1. Spinel structure. Local environments of both tetrahedral sites *A* and octahedral sites *B* are shown. Large circles represent oxygens; small circles metal cations. The large cube is the conventional unit cell. For clarity, some of the atoms are not shown.

vation requires eight +2 and sixteen +3 ions per unit cell, assuming no vacancies are present. It is important to note that although there are as many +2 ions as tetrahedral sites and as many +3 ions as octahedral sites, it does not follow that the +2 ions must reside on the tetrahedral sites and the +3 ions on the octahedral sites. In fact, it is well known that in magnetite (Fe_3O_4), the +2 ions occupy octahedral sites while the +3 ions are distributed between both kinds of site.[9]

Depending on the distribution of cations, the oxygens are usually displaced away from the tetrahedrally coordinated cations relative to the ideal fcc lattice. This displacement is conventionally specified by the oxygen parameter *u*, which is 0.375 for the undistorted (fcc) structure and generally adopts values between 0.375 and 0.390.[9] In addition, the differences in size of the constituent cations will likely introduce local distortions into the lattice.

B. EXAFS

In transmission EXAFS experiments, the x-ray absorption of the sample as a function of energy is recorded, typically using synchrotron radiation as the x-ray source. At energies from 30 to 1000 eV above an element-specific electron binding energy (''edge''), interference between the outgoing and backscattered photoelectron wave modulates the absorption. This oscillation contains information about the local scattering environment around atoms of the element, often out to more than 5 Å.

If the Fourier transform of the absorption fine structure as a function of photoelectron momentum is plotted, the result is related to the radial distribution function of scatterers about the absorbing atom. The relation is not straightforward; it is modified by several factors, including absorber- and scatterer-dependent phase shifts, the lifetime of the core hole, and truncation effects in the Fourier transform. The result is that, while peaks in the Fourier transform can be identified as being due primarily to particular shells of scattering atoms, quantitative information such as absorber-scatterer distances cannot be read directly from the Fourier-transform profile.

Two basic strategies have been used to extract quantitative information from the EXAFS Fourier transform. First, comparison to empirical standards can be used. If the Fourier transform of the EXAFS of a well-characterized material is compared to the Fourier transform of the EXAFS of a sample believed to be similar, differences in the spectra can be explained in terms of difference in bond lengths, site occupancies, Debye-Waller factors, and the like.

The second strategy is to calculate the spectrum of a model structure *ab initio* (a ''theoretical standard''). The theoretical standard is then modified by allowing parameters of interest to vary; these parameters are optimized by performing a least-squares fit to the data. The agreement between the fit and the data is indicative of the validity of the model; if the model is found to be valid the values of the fitted parameters are then considered to be accurate.

Both the strategies have disadvantages. Comparison to empirical standards is often only semiquantitative, may leave open the question of the origin of a difference in spectra, and does not account for differences in multiple-scattering contributions. Theoretical standards, on the other hand, may suffer from systematic errors in the initial choice of model structure, the choice of fitted parameters, and in the assumptions intrinsic to the *ab initio* computation.

In practice, a combination of both techniques has been found to be effective. Data is collected on an empirical standard as well as the experimental sample. A theoretical standard is then calculated, and similar fits are performed to the spectra of both the empirical standard and the experimental sample. The fit quality and parameter values for the two fits are then compared to yield information about the experimental sample and the validity of the model. In this way, systematic errors introduced by the theoretical standard and choice of fitting parameters will affect both sets of fitted parameters in similar ways, leading to a quantitative, accurate determination of the structure of the experimental sample.

Previous EXAFS analyses of mixed ferrites such as MZFO have employed a variety of techniques, including qualitative comparison of a series to an empirical standard,[10–18] qualitative comparison of a series to a theoretical standard,[8,10,15] determination of site occupancy by fitting to a theoretical standard,[11,12,18,19] determination of bond lengths by fitting to a theoretical standard,[16] and determination of bond lengths, coordination numbers, and Debye-Waller factors by fitting to empirical standards.[17] These studies analyzed each edge separately, and were generally able to focus only on one or two structural parameters, assuming that the rest were similar to the bulk. In Ref. 17, although more parameters were allowed to vary, only elements that were restricted to a single first-shell oxygen distance (and thus a single type of site) could be unambiguously fit.

In this work, spectra are collected on all three of the transition-metal *K* edges, and a theoretical standard built for each edge. The fits to all three edges are then refined simultaneously, taking full advantage of the redundant information inherent in having access to three local environments. This technique has previously been applied to find structural parameters for $Pb_{1-x}Ge_xTe$,[20] as well as for arsenate and chromate bound to self-assembled monolayers on mesoporous supports.[21]

III. EXPERIMENT

A. Synthesis

The nanoparticles used in this study were produced by the reverse micellar method.[22] For this synthesis, a solution comprising a hydrocarbon, water, and a surfactant was used to form the micelles; $FeCl_2$, $ZnCl_2$, and $MnCl_2$ were used to provide the metal cations; and ammonium hydroxide was used to precipitate a mixed metal hydroxide. The amount of starting materials was such that the relative amounts of manganese, zinc, and iron were 1:1:4.

Two different surfactant systems were used. For the samples henceforth referred to as type *A*, bis-(2-ethylhexl) sodium sulfosuccinate, a twin-tailed anionic surfactant dissolved in 2, 2, 4-trimethylpentane was used. For samples of type *B*, the surfactant was a mixture of nonylphenol poly(oxyethylene)$_5$ (NP-5) and nonylphenol

TABLE I. Results of preliminary probes. Uncertainties in the least significant digit are given in parentheses. ICP: relative stoichiometry of metals, normalized to total of 3.0 for comparison with conventional ferrite formula (AB_2O_4). XRD purity: phase purity as determined by x-ray diffraction (see Sec. III B). Size: Crystallite size as determined by Scherrer analysis and particle size as determined by DLS.

Sample	S_1	S_2	S_3	A_1	A_2	B_1	B_2
ICP:							
Manganese	0.71(3)	0.54(3)	0.55(3)	0.66(3)	0.68(3)	0.65(3)	0.64(3)
Zinc	0.76(3)	0.52(3)	0.52(3)	0.21(3)	0.25(3)	0.36(3)	0.38(3)
Iron	1.53(3)	1.94(3)	1.93(3)	2.13(3)	2.07(3)	1.99(3)	1.98(3)
XRD purity	Good	Poor	Good	Poor	Good	Good	Fair
Size (nm):							
Scherrer				12.9(6)	14.6(21)	10.8(9)	11.5(11)
DLS				34(5)	34(5)	30(5)	33(5)

poly(oxyethylene)$_9$ (NP-9); NP-5 and NP-9 are nonionic surfactants dissolved in cyclohexane.

All nanoparticle samples were fired for 5 h under nitrogen to drive off the coordinated water and facilitate the conversion and oxidation of the methal hydroxides to the spinel ferrite; those of type *A* at 525 °C and those of type *B* at 500 °C.

The standards were synthesized by a traditional ceramic method, as described in Ref. 13. For standard S_1, MnO, ZnO, and α-Fe_2O_3 underwent five cycles of ball milling and firing for 20 h at 1150 °C. The ratio of starting materials for this sample was chosen to give a product stoichiometry of $Mn_{0.67}Zn_{0.67}Fe_{1.67}O_4$. In conjunction with standard S_3 (*vide infra*), this standard provides information on the effect of stoichiometry on structural parameters.

Standard S_2 was synthesized to contain significant amounts of phase impurities so that the effect of these impurities on the fit could be ascertained. For sample S_2, Mn_2O_3, ZnO, and α-Fe_2O_3 were ball milled and then fired for a single 20-h period at 1200 °C. The ratio of starting materials was chosen to give a product stoichiometry of $Mn_{0.5}Zn_{0.5}Fe_2O_4$.

Standard S_2 was then subjected to four additional cycles of ball milling and 20-h firings at 1200 °C, with the product designated sample S_3. This was expected to produce a pure sample of $Mn_{0.5}Zn_{0.5}Fe_2O_4$.

B. Preliminary structural probes

The stoichiometry of each sample was determined by ICP. The results are summarized in Table I, normalized to a total of three metal atoms per formula unit (for easy comparison with the stoichiometry of other ferrites). The experimental uncertainty of 0.03 was estimated by calculating the standard deviation of multiple runs performed on some of the samples. As can be seen, each synthetic protocol yielded a consistent stoichiometry, with the samples of type *A* showing consistently more zinc loss than those of type *B*.

A diffractogram of each sample was collected on a Phillips PW1710 powder diffractometer. Results are shown in Fig. 2. As anticipated, standard S_2 shows features not found in S_1 or S_3 due to the presence of other oxide phases. In addition, sample A_1 shows broad shoulders on some of the peaks, indicating the presence of a phase impurity with low to moderate long-range order. Sample B_2 also shows one sharp peak that is not present in S_1. The sharpness of the peak relative to other features in the nanoparticle diffractograms suggests the presence of a small amount of a secondary phase with crystallite size considerably larger than the MZFO nanoparticles. The other diffractograms are consistent with pure-phase MZFO, although amorphous impurities cannot be ruled out by this method.

The mean size of the particles was estimated by two methods: Scherrer analysis of the broadening of the peaks in the diffractogram, and dynamic light scattering (DLS). It should be noted that the Scherrer analysis neglects other contributions to broadening, such as local disorder and strain. As such, it provides a lower bound on the particle size. DLS, on the other hand, may be subject to particle aggregation, and thus provides an upper bound on the size. The results of both probes are summarized in Table I. As can be seen, both methods suggest that all four samples contain particles with similar average size, although Scherrer analysis suggests the samples of type *A* may have a slightly larger crystallite size than type *B*.

C. X-ray-absorption spectra

Samples were prepared by grinding the sintered powder in a mortar and pestle, and then spreading thin layers of finely ground powder on multiple layers of Kapton tape. The number of layers of tape was chosen so that the total absorption would be from one to four absorption lengths at all edges. Uniformity was confirmed at the beam line by measuring transmission as a function of the beam position.

Data was collected at beam lines *X*11*A* and *X*23*B* of the National Synchrotron Light Source at Brookhaven National Laboratory. Both beam lines use double-crystal monochromators. Harmonic rejection on *X*11*A* is attained by detuning the optics so that the intensity of the incident beam is reduced by approximately 25%; on *X*23*B*, the downstream focusing mirror provides harmonic rejection.[23] In all cases, at least two scans were averaged at each edge of each sample.

The two beam lines have somewhat different characteristics. The focusing mirrors on *X*23*B* provide much higher flux, and thus better counting statistics. On the other hand,

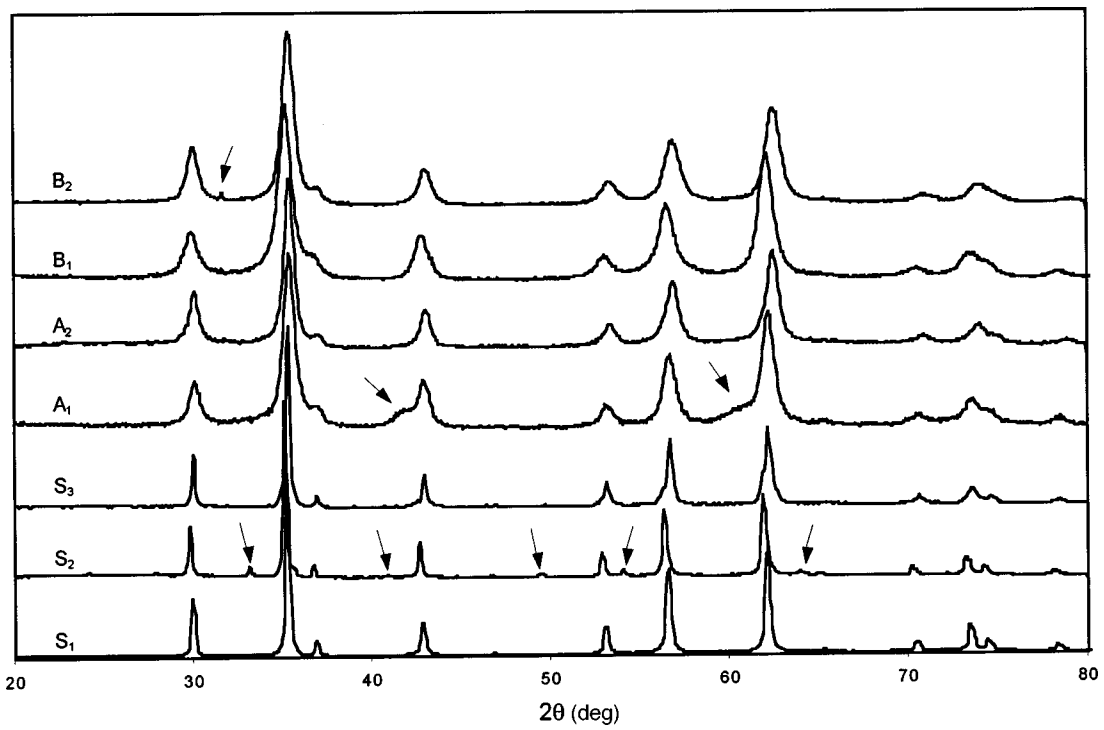

FIG. 2. X-ray diffractograms of standards and samples (identified at left). Arrows show features not present in standard S_3.

the mirrors also tend to limit the useful energy range that can be sampled in one spectrum. Thus $X23B$ could be expected to provide higher quality data, while $X11A$ samples a greater range of energy space. The spectra of some samples were collected on both lines to provide a check on the reliability of the analysis.

D. Magnetic measurements

Subsequent to completion of the EXAFS analysis, hysteresis loops at 10 and 300 K were collected on a quantum design magnetic property measurement system 5*S* superconducting quantum interference device magnetometer. Results are shown in Fig. 3, with the insets showing an expanded view of the low-field portion of the loops. As can be seen, sample B_1 shows markedly different behavior from the other nanoparticle samples (but similar to standard S_1) despite using the same synthetic protocol as sample B_2. As detailed in Sec. III B, B_1 and B_2 have similar stoichiometry and particle size. Likewise, their diffractograms exhibit only small differences. In light of the results of the EXAFS analysis (see Sec. V), this suggests that the magnetic differences between B_1 and B_2 are due to a difference in cation distribution.

The hysteresis loops of samples A_1 and A_2 show similar differences, but they are less pronounced than the differences between the samples of type *B*.

The low saturation moment of S_1 relative to S_3 is a well-known consequence of the excess of diamagnetic zinc ions in S_1.[1,9]

IV. ANALYSIS

A. Background subtraction

Non-EXAFS (''background'') contributions to the absorption spectrum are generally assumed to be slowly varying functions in energy. Contributions to the background include the absorption that would be present for an isolated atom of the absorbing element (''atomic absorption''), absorption due to other elements in the sample, absorption due to other materials in the beam path such as windows and gases, and instrumental effects. Much attention in the literature has been focused on the first of these mechanisms (Ref. 24 provides a survey), but the other mechanisms may also contribute significantly, particularly for samples with multiple elements of similar atomic number.

For the purpose of background removal, the contributions may be grouped into two categories: absorption due to the electron taking part in the formation and decay of the core hole (''intrinsic background'' μ_i) and absorption due to other electrons, including those in other elements (''extrinsic background'' μ_e). Note that the atomic background comprises the intrinsic background as well as contributions to the extrinsic background.

The measured absorption μ is given by

$$\mu = \mu_e + \mu_i(1+\chi), \tag{1}$$

where χ is the EXAFS and all variables are a function of energy. *Subtracting* a background, regardless of the function used, thus introduces an energy-dependent normalization error to χ. The effect is relatively small, however, and can be approximated by considering tabulated atomic absorptions. In this study, background subtraction is performed using the method of Newville *et al.*,[25] followed by a normalization correction based on the data of McMaster *et al.*[26]

For all spectra, a background spline was chosen that minimized the difference of the Fourier transform from a spectrum calculated *ab initio* below 0.9 Å. In the case of the iron edge of sample S_3, the resultant spline exhibited large non-

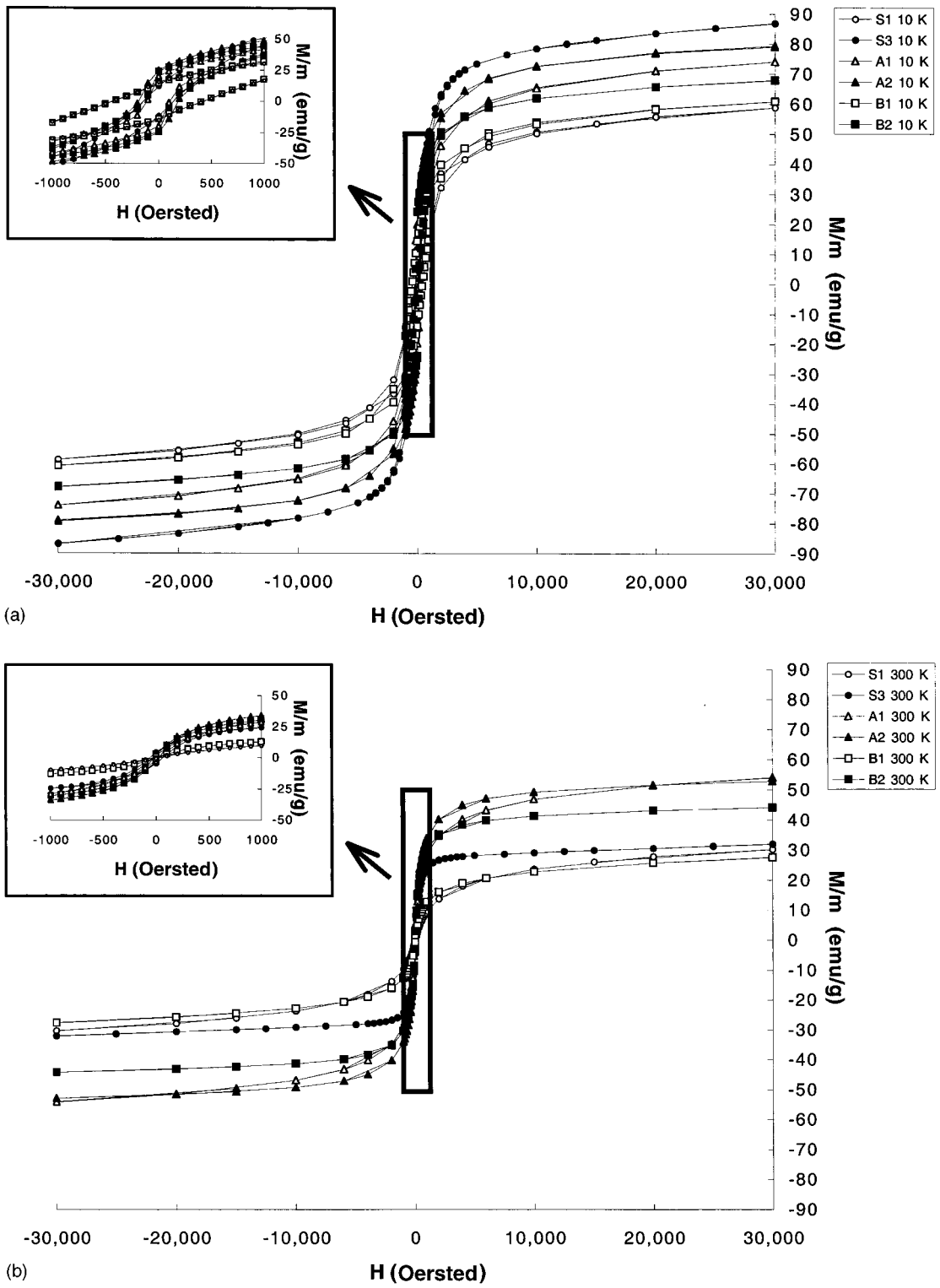

FIG. 3. Hysteresis loops: (a) 10 K; (b) 300 K. Insets show expanded view of low-field loops.

physical features; the threshold for this spectrum was reduced to 0.8 Å, causing the artifacts to disappear. A typical background function is shown in Fig. 4.

B. Data selection

After background subtraction, data was transformed to a function of photoelectron wave number k. Since EXAFS amplitude generally falls off with increasing k, the data was multiplied by k prior to taking the Fourier transform. Spectra are shown in Fig. 5. In the case of data collected on beam line $X23B$, artifacts generally preclude the use of data above 14 $Å^{-1}$. For data from $X11A$, data is often usable up to a few eV from the maximum collected, at which point artifacts stemming from the termination of the background spline be-

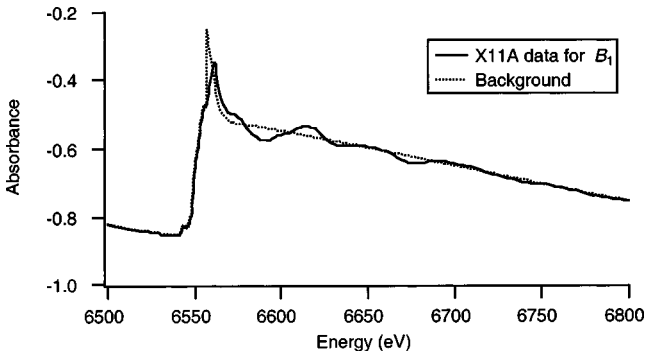

FIG. 4. Manganese edge and background for sample B_1 data collected on beam line *X*11*A*. Termination artifact below 6575 eV is not within fitting range.

come dominant. In addition, it is well known that low-*k* data is dominated by non-EXAFS processes.[27] Thus it is appropriate to use a subset of the data for the Fourier transform.

It was found that, in general, both the value of parameters resulting from fits and the statistical quality of the fits were stable over a range of *k* space. Outside of that range, the statistical quality of the fits often dropped rapidly. The *k* ranges selected are as large as possible consistent with fits of good statistical quality, and are given in Table II.

It is worth noting that in some cases the maximum of the *k* ranges selected are below 10.0 $Å^{-1}$, unusually low for EXAFS studies. For the manganese spectrum this is due to the presence of the iron edge. In other cases, however, it may indicate a limitation of the model (see discussion in Sec. IV D).

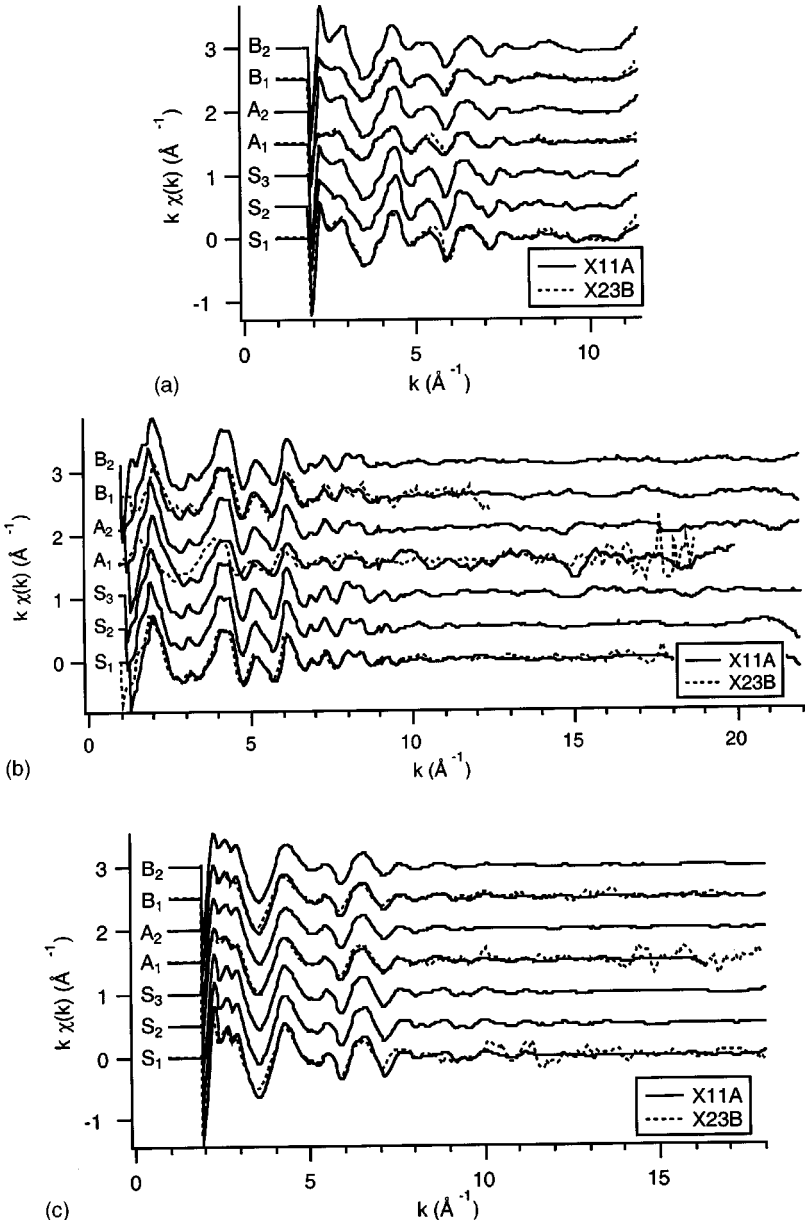

FIG. 5. EXAFS spectra: (a) manganese *K* edge; (b) zinc *K* edge; (c) iron *K* edge. Spectra have been translated vertically for clarity. Samples are identified at left; when data was collected on the same sample at both beam lines, the spectra are superimposed with the *X*23*B* data being shown as a dotted line.

TABLE II. EXAFS statistical data. The columns contain, respectively, sample identifiers; NSLS beam lines on which data was collected; ranges of data used for Fourier transforms associated with Mn, Zn, and Fe edges; numbers of independent points according to Eq. (5); numbers of degrees of freedom according to Eq. (4); EXAFS $\mathcal{R}$ factors for Mn, Zn, and Fe edges; and χ^2_ν for the fit calculated as described in Sec. IV F.

Sample	Line	Mn k (Å^{-1})	Zn k (Å^{-1})	Fe k (Å^{-1})	N_{idp}	ν	R_{Mn}	R_{Zn}	R_{Fe}	χ^2_ν
S_1	*X*23*B*	3.0–8.0	3.0–13.0	3.0–9.0	64	48	0.019	0.031	0.037	747
	*X*11*A*	3.0–9.5	3.0–20.0	3.0–17.0	110	94	0.038	0.035	0.035	548
S_2	*X*11*A*	3.0–8.0	3.0–20.0	3.0–17.0	106	90	0.069	0.033	0.039	581
S_3	*X*11*A*	3.0–7.5	3.5–14.0	3.0–16.0	84	68	0.045	0.026	0.039	1447
A_1	*X*23*B*	3.0–8.0	3.0–9.0	3.5–9.0	53	37	0.102	0.025	0.044	896
	*X*11*A*	3.0–8.0	3.0–9.0	3.0–12.0	61	45	0.128	0.023	0.043	2989
A_2	*X*11*A*	3.0–8.0	3.0–12.0	3.0–8.0	58	42	0.036	0.037	0.054	3085
B_1	*X*23*B*	3.0–7.5	4.0–8.0	3.0–8.0	43	27	0.047	0.039	0.036	1772
	*X*11*A*	3.0–7.5	3.0–13.0	3.0–13.0	74	58	0.049	0.023	0.047	1896
B_2	*X*11*A*	3.0–8.0	4.0–18.0	3.0–8.0	73	57	0.037	0.034	0.058	1836

Within the ranges chosen, the manganese edge shows the greatest differences between samples, followed by the zinc edge. The phase differences evident between some of the zinc spectra, such as the *X*11*A* and *X*23*B* spectra of sample A_1, are attributable to the difficulty of choosing an energy origin on the zinc edge. This artifact was compensated for by allowing ΔE_0 to vary during the fitting process.

All Fourier transforms were performed with Hanning windows with sills of size 1.0 Å^{-1} to reduce data truncation effects. Note that this means data is sampled from a region that extends 0.5 Å^{-1} to each side of the nominal ranges given in Table II.

Once identical Fourier transforms had been performed on the data and the theoretical standard, fitting was performed over the uncorrected distance 1.0–5.5 Å. This range was chosen to extend from just above the background region to a distance encompassing multiple shells of cations.

C. Theoretical standards

Theoretical standards for this study were generated by performing *ab initio* calculations using FEFF8.[28] A cubic spinel structure (space group $Fd3m$) was used, with most of the tetrahedral sites occupied by zinc cations and most of the octahedral sites occupied by manganese and iron cations. No vacancies were allowed. Lattice and oxygen parameters were based on Ref. 29. A standard was calculated for the tetrahedral and octahedral environments for each of the three cations, leading to six standards.

To improve the estimate of the inner potential E_0, a self-consistent field calculation to a distance of 5.0 Å was used.

D. Constraints

Given the number of significant scattering paths within the fitting range, there are easily hundreds of parameters that could be varied in order to fit the theoretical standards to the data. Given the limited amount of information available in the Fourier transforms (see Sec. IV B), this is an underdetermined problem. To reduce the number of parameters fit, several classes of constraints were used:

(1) Self-consistency: Some constraints are required in order to generate a consistent structure. For example, the distance from a zinc cation in a tetrahedral site to a manganese cation in an octahedral site must be the same whether determined from the zinc or from the manganese.

(2) Stoichiometry: ICP determinations of the stoichiometry were used to constrain the site occupancies of the cations. For example, if the fractions of manganese and zinc in tetrahedral sites were fitted, the fraction of iron in tetrahedral sites could be calculated.

(3) Multiple scattering: All multiple-scattering paths were constrained in terms of direct scatterers, using the scheme described in Ref. 30. This scheme treats the thermal motion of different atoms as uncorrelated, but does account properly for ''double'' multiple-scattering paths, in which the same atom acts as a scattering center twice.

(4) Phase purity: No oxides or other impurities were allowed in the final fits.

(5) Vacancy: It was assumed that no vacancies were present.

(6) Gaussian disorder: Pair distribution functions were assumed to be harmonic.

(7) Cation distribution: It was assumed that once the distribution of cations between tetrahedral and octahedral sites was determined, the distribution within those sites was random. For example, it was assumed that the zinc-filled octahedral sites were neither more nor less likely to be near iron cations than the manganese- or iron-filled octahedral sites.

(8) Valence distribution: No allowance was made for the presence of +2 and +3 ions in equivalent sites. For example, only one bond length was allowed for the first-shell octahedral-site manganese-oxygen bonds; if +2 and +3 manganese ions were both present in octahedral sites, then two distinct bond lengths would be expected.

(9) Element dependence of first coordination shells: mean-square displacements (MSD's) and fractional changes in first-shell metal-oxygen distances were assumed to be the same for octahedral and tetrahedral sites occupied by the same element (e.g., iron in octahedral and iron in tetrahedral).

(10) Uniformity of outer coordination shells: All coordination shells beyond the first one were assumed to yield the same MSD's, regardless of the absorbing element. Likewise, the locations of scatterers in coordination shells beyond the first one were assumed to be determined solely by the lattice and oxygen parameters; i.e., they are not species dependent.

(11) Homogeneity: It was assumed that any disorder or defects present were distributed uniformly throughout the material.

Constraints (4)–(11) represent simplifications relative to the real structure, and are likely to be responsible for the disagreement with the data at high photoelectron wave number. Constraints (4) (in the form of binary oxides), (6) (in the form of nonzero third cumulants), (8), and (9) were explored; relaxing (4) and (6) did not yield parameters different from the constraints to within the uncertainties of the fit, relaxing (8) and (9) produced large uncertainties and correlations between variables without significantly improving the statistical quality of the fit.

Constraint (11), while reasonable for the ceramic samples, is likely to be somewhat inaccurate for the nanoparticles. Surface effects are more important for the nanoparticles, and there may be radial gradients in structural parameters (e.g., the interatomic distance may increase from the center of the particle toward the surface). Nevertheless, these effects should be of only modest importance, since in a 10-nm-radius particle, more than 90% of the atoms lie two or more monolayers below the surface. The primary consequence of neglecting surface effects would be to lower the amplitude of the EXAFS oscillations relative to the total absorption (surface atoms have fewer neighbors), while the effect of modest radial gradients would be primarily to increase MSD's.

In summary, the following parameters were allowed to vary:

(1) Overall lattice parameter a.

(2) Oxygen parameter u.

(3) Fractional difference in the distance between manganese and oxygen, and zinc and oxygen in the first coordination shell, as compared with the distances implied by a and u. The fractional difference for iron was then calculated from the stoichiometry and from the manganese and zinc values (two parameters).

(4) MSD for each metal with its first-coordination-shell oxygens (three parameters).

(5) MSD for all outer-shell paths.

(6) Site occupancy of zinc and manganese. Iron occupancy was then determined from the stoichiometry and the zinc and manganese occupancies (two parameters).

(7) Amplitude reduction factor S_0^2 for each element (standard EXAFS parameter). Properly, this factor accounts for multielectron processes. In this case, it is also likely to incorporate surface effects in the nanoparticles (three parameters).

(8) Inner potential shift ΔE_0 for each edge (standard EXAFS parameter) (three parameters).

There were thus a total of 16 parameters fitted.

E. Analysis of uncertainties

To evaluate the quality of fits, two metrics are commonly used: EXAFS $\mathcal{R}$ factor and χ_ν^2.

The EXAFS $\mathcal{R}$ factor is a measure of the fractional difference between data and fit:

$$\mathcal{R}=\frac{\Sigma_i(\tilde{\chi}_{\mathrm{fit}}(r_i;\ \text{varied parameters})-\tilde{\chi}_{\mathrm{data}}(r_i))^2}{\Sigma_i(\tilde{\chi}_{\mathrm{data}}(r_i))^2}, \quad (2)$$

where the r_i are equally spaced points in the complex Fourier transform. Values below 0.02 are typically considered to be good; values between 0.02 and 0.05 indicate some mismatch between fit and data, but are still widely considered to be acceptable.

The χ_ν^2 attempts to measure the difference between fit and data relative to the uncertainties in the data. It is defined by the equation

$$\chi_\nu^2=\left(\frac{1}{\nu}\right)\left(\frac{N_{idp}}{N}\right)\times\sum_{i=1}^{N}\left(\frac{(\tilde{\chi}_{\mathrm{fit}}(r_i;\ \text{varied parameters})-\tilde{\chi}_{\mathrm{data}}(r_i))}{\varepsilon_i}\right)^2, \quad (3)$$

where

$$\nu=N_{idp}-N_p; \quad (4)$$

and N_{idp}, N_p, and ε are the number of independent data points, number of fitted parameters, and the uncertainty in the Fourier-transformed data, respectively. Although this definition is consistent with established statistical usage, it is difficult to determine in practice, because ε and, to a lesser extent, N_{idp} are not generally known.

In the absence of better estimates of ε, the fluctuations in the Fourier transform between 15 and 25 Å are often used to provide an estimate. This is appropriate if two conditions are met: the noise must dominate over structural information in that range; and the noise must be ''white,'' i.e., it must be the same at all frequencies. Although the former is generally a good assumption, the latter may not be. For example, the feedback systems used to keep the x-ray beam at the same location on the sample may introduce error over some frequency ranges but not others.

A straightforward application of information theory gives

$$N_{idp}=\frac{2\Sigma_i\Delta r_i\Delta k_i}{\pi}+1, \quad (5)$$

where Δk and Δr are, respectively, the data selection and fitting ranges; and the sum is over independent spectra (such as those from different elements). It has recently been pointed out that this formula gives the amount of information

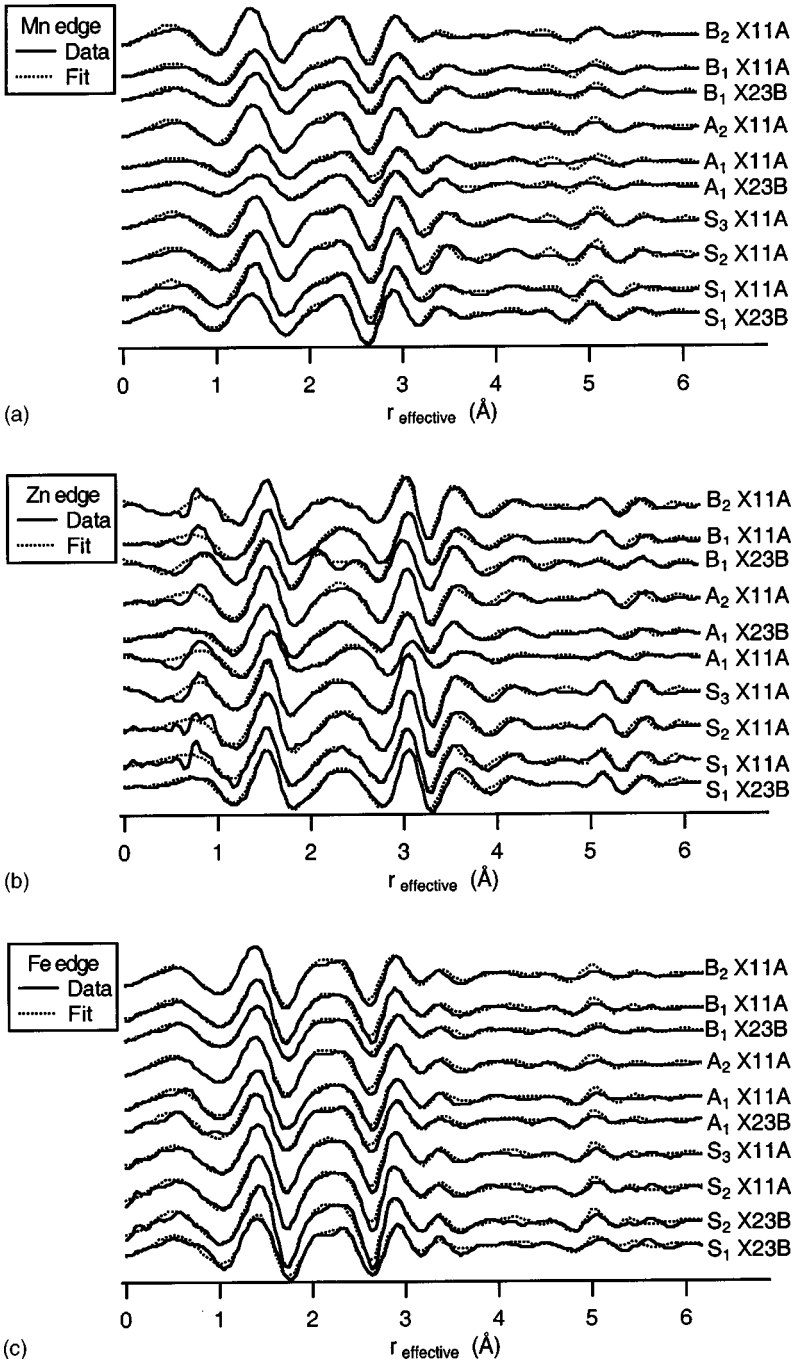

FIG. 6. Real part of Fourier transform of EXAFS data and fits: (a) manganese edge; (b) zinc edge; (c) iron edge. Sample and beam line is given at right.

in an ''ideally packed'' signal.[31] Since EXAFS is not ideally packed, the number of independent points may be considerably smaller than predicted by this formula.

It is worth noting that χ^2_ν is typically used for two distinct purposes: it is the quantity minimized in the fitting process and it also provides an estimate of the quality of the fit relative to the uncertainty in the data. The requirements of the two are different: for the former, which is used to arrive at the best-fit values for structural parameters, it would be appropriate to use an ε that includes errors in the model, such as those discussed in the preceding section. For the latter, which is meant to measure the accuracy of the model, ε should include only factors such as measurement noise. For the materials described in this paper it is expected that errors due to the constrained model dominate over other sources of error. Thus, for purposes of achieving the best fit, the ε for all spectra (as measured in k space) have been forced to the same value; i.e., all k-space data is considered to have the same weight in the fit. For the purpose of estimating fit quality relative to experimental uncertainty, however, the ε for each spectrum has been estimated in the manner described in the previous paragraph, and Eq. (5) has been used to estimate the number of independent points. This allows for comparison to other EXAFS literature.

Uncertainties in fitted parameters were calculated using the method in Ref. 32; in brief, this method provides conservative estimates of the uncertainties that are independent of ε.

TABLE III. Results of fitting EXAFS data to a theoretical standard. Uncertainties in the least significant digit are given in parentheses.

	S_1	S_2	S_3	A_1	A_2	B_1	B_2	Line
Lattice parameter (Å)	8.52(2)		NS[a]	NS[a]		8.59(4)		*X23B*
	NS[a]	8.54(2)[b]		8.52(3)[b]	8.52(3)[b]	NS[a]	8.50(3)[b]	*X11A*
Oxygen	0.387(3)			0.382(6)		0.386(7)		*X23B*
parameter	0.382(2)	0.381(4)	0.381(4)	0.384(6)[b]	0.383(5)	0.381(4)[b]	0.387(4)	*X11A*
S_0^2:								
Manganese	1.13(9)			0.74(11)		0.83(12)		*X23B*
	NS[a]	0.98(7)	1.00(7)	0.66(9)	0.99(11)	0.80(7)	1.09(12)[b]	*X11A*
Zinc	1.19(10)			0.77(10)		NS[a]		*X23B*
	1.07(8)	1.21(12)	1.22(11)	0.88(10)	1.24(15)	1.11(10)	1.44(22)	*X11A*
Iron	1.01(8)[b]			0.96(10)[b]		0.87(11)[b]		*X23B*
	1.10(7)	1.04(9)	0.99(9)	1.00(12)[b]	1.06(11)[b]	1.01(9)[b]	1.12(10)[b]	*X11A*
Tetrahedral (%):								
Manganese	15(5)			42(11)		47(12)		*X23B*
	18(4)	47(6)	39(6)	50(11)	34(9)	38(7)	14(8)	*X11A*
Zinc	100(7)			85(14)		NS[a]		*X23B*
	96(6)	97(9)	99(9)	89(11)	100(11)	100(6)	100(16)	*X11A*
Iron	9(4)			26(3)		NS[a]		*X23B*
(Calculated)	9(4)	12(3)	14(4)	23(3)	25(3)	17(3)	27(5)	*X11A*
First-shell distortion:								
Manganese	0.005(5)			0.034(10)		0.007(8)		*X23B*
	−0.008(3)	0.004(4)	−0.002(4)	0.012(7)	−0.004(6)	−0.003(5)	−0.016(6)	*X11A*
Zinc	−0.002(7)			0.002(10)		NS[a]		*X23B*
	0.008(6)	0.006(9)	0.004(9)	−0.003(9)[b]	0.011(11)	0.013(8)	0.003(11)	*X11A*
Iron	−0.001(6)			−0.011(4)		NS[a]		*X23B*
(Calculated)	0.000(4)	−0.003(4)		−0.004(3)	0.000(3)	−0.002(3)	0.005(4)	*X11A*
Outer MSD (Å^2)	0.010(1)			0.012(2)		0.012(2)		*X23B*
	0.009(1)	0.010(1)	0.009(1)	0.012(2)	0.013(2)	0.012(1)	0.013(1)	*X11A*
First-shell MSD (Å^2):								
Manganese	0.027(3)			0.024(7)		0.014(5)		*X23B*
	0.015(2)	0.013(2)	0.014(2)	0.012(4)	0.016(4)	0.015(3)	0.018(3)[b]	*X11A*
Zinc	0.007(2)			0.003(3)		NS[a]		*X23B*
	0.006(2)	0.008(3)	0.007(2)	0.005(3)	0.008(3)	0.008(2)	0.009(4)	*X11A*
Iron	0.012(2)[b]			0.012(3)[b]		0.011(4)[b]		*X23B*
	0.008(2)	0.009(2)	0.010(3)	0.012(3)[b]	0.014(3)[b]	0.011(3)[b]	0.014(3)[b]	*X11A*

[a]Parameters that were not stable (NS) with respect to changes in the data range analyzed.
[b]Highly correlated variables (see Table IV).

V. RESULTS AND DISCUSSION

Fourier transforms of the data and the fitted models are given in Fig. 6, statistical data is provided in Table II, and fitted parameters are given in Table III. (Parameters that were not stable with changes in the range of *k*-space fitted are shown as NS in Table III.) Variables with correlation coefficients greater than 0.80 are noted in Table IV, and marked as footnote ''b'' in Table III.

A. Phase purity and model validity

EXAFS $\mathcal{R}$ factors between 0.02 and 0.05 are often considered indicative of a constrained model that, although essentially applicable to the sample, contains some significant differences in detail. Since in this study the fit to standards S_1 and S_3 yield $\mathcal{R}$ factors in this range, and since these standards appear to be nearly phase pure under x-ray diffraction, it is likely that the error in those cases is primarily due to constraints (5)–(10) (see Sec. IV D).

In most cases, the statistical quality of the fits is comparable to, or slightly worse than, the fits to standards S_1 and S_3. The manganese edges of standard S_2 and sample A_1 are poorly fitted by the model; these are also the samples with significant phase impurities according to XRD. Sample B_2, with a small impurity visible in XRD, exhibits the next highest $\mathcal{R}$ factor (on the iron edge). Thus it appears that the fitting process does reveal phase impurities, and that the other samples are reasonably phase pure. (The moderate degradation of fit quality for the other sample edges as compared to the standard S_1 may be due to a combination of small

TABLE IV. Correlation coefficients above 0.80 for fitted parameters.

Sample	Line			Correlation
S_1	*X*23*B*	Fe S_0^2	Fe first-shell Debye-Waller	0.80
	*X*11*A*	Mn ΔE_0	lattice parameter	0.83
S_2	*X*11*A*	Mn ΔE_0	Lattice parameter	0.88
S_3	*X*11*A*	Mn ΔE_0	Lattice parameter	0.85
		Zn ΔE_0	Lattice parameter	0.82
A_1	*X*23*B*	Fe S_0^2	Fe first-shell Debye-Waller	0.83
	*X*11*A*			0.81
	*X*11*A*	Zn ΔE_0	lattice parameter	0.85
	*X*11*A*	Oxygen parameter	Zn first-shell distortion	−0.81
A_2	*X*11*A*	Fe S_0^2	Fe first-shell Debye-Waller	0.83
	*X*11*A*	Zn ΔE_0	lattice parameter	0.82
	*X*23*B*	Zn ΔE_0	Lattice parameter	0.87
	*X*11*A*			0.82
	*X*23*B*	Zn S_0^2	Zn first-shell Debye-Waller	0.85
	*X*23*B*	Fe S_0^2	Fe first-shell Debye-Waller	0.83
	*X*11*A*			0.80
	*X*23*B*	Mn ΔE_0	lattice parameter	0.80
	*X*11*A*	Oxygen parameter	Zn first-shell distortion	−0.81
B_2	*X*11*A*	Fe S_0^2	Fe first-shell Debye-Waller	0.85
	*X*11*A*	Mn S_0^2	Mn first-shell Debye-Waller	0.81
	*X*11*A*	Fe ΔE_0	lattice parameter	0.81

amounts of impurities and deviations from the bulk structure not properly accounted for by the constrained model, e.g., surface effects and valence disorder.)

The fitted values of the EXAFS parameter S_0^2 are within typical ranges, although the values for zinc are consistently about 20% too high. EXAFS data are normalized by the jump in absorption at the edge, which is sometimes difficult to determine. In this study, the edge jump was estimated by an automated process that was identical for all samples, so that any errors present are likely to be consistent for a given edge. Normalization differences of this sort have no effect on the quality of fit or on the other EXAFS parameters.

The fitted ΔE_0 values were found relative to a subjectively chosen point on each edge. As such, the values are not meaningful for comparison, and are not given in Table III. All fitted values resulted in energy origins along the rising portion of the absorption edge.

TABLE V. Affinity of manganese for tetrahedral sites relative to iron. Uncertainties in the least significant digit are given in parentheses.

Sample	Mn tetrahedral affinity
S_1	1.4(6)
S_2	2.4(5)
S_3	2.0(5)
A_1	1.6(5)
A_2	1.2(3)
B_1	1.8(5)
B_2	0.6(4)

B. Site occupancies

The magnetic properties of ferrites are due to an antiferromagnetic coupling between the octahedral and tetrahedral sublattices. Since there are twice as many octahedral as tetrahedral sites, even a uniform distribution of magnetic ions between the sites can result in a net magnetization. Zinc is diamagnetic and shows a strong preference for tetrahedrally coordinated sites in spinels, thus the presence of zinc in a ferrite will generally suppress the moment of the tetrahedral sublattice and enhance the moment of the compound as a whole. If zinc ions occupy more than about 50% of the tetrahedrally coordinated sites, however, the antiferromagnetic coupling between the tetrahedral and octahedral lattices begins to break down, and the net magnetization decreases.[9] This effect can be seen in standard S_1.

Previous studies have shown that, despite the strong affinity of zinc cations for tetrahedrally coordinated spinel sites, attempts to synthesize low-dimensional MZFO by the coprecipitation,[16] pulsed-laser deposition,[12] and high-energy ball-milling methods[12,13] all may yield significant amounts of zinc in the octahedrally coordinated sites. Harris *et al.*[12] suggest that this may be associated with a modification of the surface structure, possibly accompanied by oxidation of manganese ions and the formation of new vacancies at tetrahedral sites. In any case, the presence of diamagnetic ions on the *octahedral* lattice, even in small amounts, would reduce the difference between the magnetization of the octahedral and tetrahedral sublattices. Since this in turn reduces the net magnetization of the material, it is not desirable for technological applications. In this study, for all standards and samples, the occupancy of zinc cations in octahedral sites is

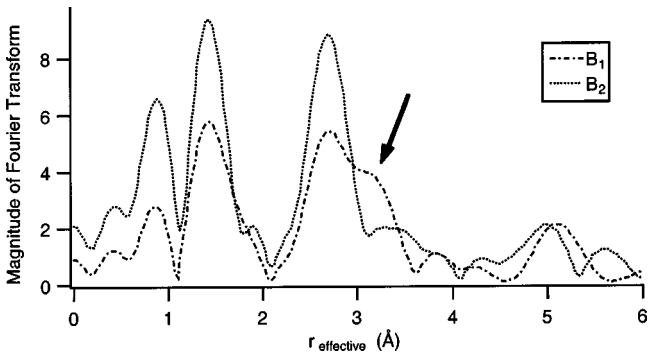

FIG. 7. Magnitude of Fourier transform (k-weight of 3) of manganese edge for samples B_1 and B_2. Arrow shows a feature characteristic of occupancy in tetrahedral sites.

smaller than the precision of the analysis, although there are indications that sample A_1 may have 10–15 % of its zinc cations in octahedral sites (this may also be due to the phase impurities in this sample).

Since the stoichiometry of the samples differ, it is informative to normalize the tetrahedral site occupancy of the manganese cations by the fraction of manganese and iron sites, which are tetrahedral. This, in effect, gives the affinity of manganese for tetrahedral sites relative to iron, with a completely random distribution yielding an affinity of 1.0. The results are presented in Table V. Harris[18] previously used neutron diffraction to find a distribution corresponding to an affinity of 2.1 for a ceramic standard; this is in good agreement with the similarly prepared standard S_3. It can be seen that the affinity of manganese for tetrahedral sites is somewhat lower in standard S_1 than in standard S_3, although the difference is not much larger than the uncertainty in the measurements. This is in agreement with the qualitative study by Dorsey *et al.*,[8] who found that, for MZFO films formed by pulsed-laser deposition, as the proportion of manganese to iron increases, the affinity of the manganese ions for tetrahedral sites decreases.

Surprisingly, significant differences in affinity are seen between samples prepared in the same way; in particular, the manganese ions in sample B_2 have much lower affinity for tetrahedral sites than those in sample B_1. (There also appears to be a difference between samples A_1 and A_2, although it does not reach the level of statistical significance.) To verify this result, the magnitude of the Fourier transforms of samples B_1 and B_2 have been plotted in Fig. 7. Dorsey *et al.*[8] and Harris *et al.*[10] established that the peak near 2.7 Å (uncorrected) is primarily due to absorbers in octahedrally coordinated sites, while the peak near 3.2 Å (uncorrected) is primarily due to absorbers in tetrahedrally coordinated sites. (The data from $k=0$ to $k=11\ \text{Å}^{-1}$ was selected and weighted by k^3 to facilitate comparison with Refs. 8–19.) It can be clearly seen that sample B_2 has relatively less tetrahedral occupation than B_1, in agreement with the quantitative analysis. Subsequently, these samples were also found to differ sharply in their magnetic characteristics (see Sec. III D).

The origin of this difference between samples prepared under the same protocol is not clear. The site occupancy may be strongly dependent on reaction conditions, such as pH.[15] Although the samples were prepared from the same reagents, the syntheses were made 5 months apart, and it is conceivable that the pH of the ammonium hydroxide may have deviated by as much as 0.2 over that period. Likewise, the $FeCl_2$ starting material shows some variation in color, suggesting oxidation to $FeCl_3$ and Fe_2O_3 may have occurred during that time. In any case, further research will be needed to determine the origin of the difference in manganese distribution between samples.

C. Mean-square displacements

It should be noted that EXAFS MSD's are distinct from Debye-Waller factors as defined for x-ray diffraction: the former are the variances in absorber-scatterer distance, while the latter are the variances in atomic positions relative to lattice points. In the absence of other effects, the tendency under ordinary conditions for adjacent atoms to move in phase (''acoustically'') tends to produce smaller MSD's for the first coordination shell than for absorber-scatterer pairs with greater separation. The analysis reveals this to be the case for all samples when the absorber is zinc, but for iron the first-shell MSD is comparable to that for the outer shells, and for manganese it is in all cases somewhat larger.

One explanation for this behavior is valence disorder. Since zinc cations must be $+2$ in all cases, the first-shell zinc-oxygen distance in each type of site would be well modeled by a Gaussian centered on a single distance. If manganese existed as both $+2$ and $+3$ ions in the same kind of site (e.g., octahedral), then the first-shell manganese-oxygen distance distribution would be better modeled by two Gaussians for each site, one for the Mn^{2+}-O distance and one for the Mn^{3+}-O distance. It is thus possible that the first-shell MSD's in these analyses are a marker for valence disorder, so that in all samples manganese shows more of this kind of disorder than iron, which in turn shows more disorder than zinc.

Alternatively, the relatively large MSD's for manganese may be related to the site disorder discussed in the preceding section, or to defects such as vacancies in the oxygen sublattice.

D. First-shell distortion

In Table III, first-shell distortions are given as a fractional difference between the particular first-shell cation-oxygen distance and the average value implied by the lattice and oxygen parameters. They were not generally well determined, showing large uncertainties relative to the differences seen. This is not surprising, as constraints (8) and (9) in Sec. IV D are not likely to provide realistic models of the first-shell distortions. More realistic models, however, yielded values that were highly correlated and uncertain.

There is a tendency for zinc to have a larger first-shell distance than that implied by the lattice and oxygen constants. This is consistent with the presence of iron and manganese in valences of both $+2$ and $+3$ in the same sites, since Fe^{3+} and Mn^{3+} are considerably smaller than Zn^{2+}, while Fe^{2+} and Mn^{2+} are only slightly larger than Zn^{2+}.[33]

VI. CONCLUSIONS

We have analyzed the x-ray-absorption fine structure of the iron, manganese, and zinc spectra of a series of manganese zinc ferrite nanoparticles synthesized by the reverse micellar technique. All edges were simultaneously fitted to a constrained model based on theoretical standards, leading to quantitative results for site occupancy, MSD's, and other parameters of interest. As a check, the same procedure was applied to empirical standards made by a conventional ceramic method. In all cases, the zinc cations were found to reside predominantly in the tetrahedral sites. The site occupancy of the manganese cations was consistent with previous studies for the empirical standards, but showed significant variations between nanoparticle samples. For samples with similar stoichiometry, this variation in manganese distribution was found to be correlated to differences in magnetic properties. In addition, MSD's were found to be significantly higher for the manganese-oxygen bonds than for the zinc-oxygen bonds, with all other interactions taking on intermediate values.

*Email address: SCalvin100@aol.com

[1] *Handbook of Microwave Ferrite Materials*, edited by Wilhelm H. von Aulock (Academic, New York, 1965), Sec. III.
[2] Z. X. Tang, C. M. Sorensen, K. J. Klabunde, and G. C. Hadjipanayis, Phys. Rev. Lett. **67**, 3602 (1991).
[3] C. Liu and Z. J. Zhang, Chem. Mater. **13**, 2092 (2001).
[4] P. J. van der Zaag, A. Noordermeer, M. T. Johnson, and P. F. Bongers, Phys. Rev. Lett. **68**, 3112 (1992).
[5] V. A. M. Brabers, Phys. Rev. Lett. **68**, 3113 (1992).
[6] P. J. van der Zaag, V. A. M. Brabers, M. T. Johnson, A. Noordermeer, and P. F. Bongers, Phys. Rev. B **51**, 12 009 (1995).
[7] Chandana Rath, S. Anand, R. P. Das, K. K. Sahu, S. D. Kulkarni, S. K. Date, and N. C. Mishra, J. Appl. Phys. **91**, 2211 (2002).
[8] P. C. Dorsey, V. G. Harris, D. B. Chrisey, P. Lubitz, J. S. Horowitz, and N. C. Koon, in *Applications of Synchrotron Radiation Techniques to Materials Science*, edited by D. L. Perry, N. Shinn, K. D. Amico, G. Ice, and L. Terminello, Mater. Res. Soc. Symp. Proc. No. 375 (Materials Research Society, Pittsburgh, 1995), p. 33.
[9] J. Smit and H. P. J. Wijn, *Ferrites* (Wiley, New York, 1959), Chap. VIII.
[10] V. G. Harris, N. C. Koon, C. M. Williams, Q. Zhang, M. Abe, and J. Kirkland, IEEE Trans. Magn. **31**, 3473 (1995).
[11] V. G. Harris, N. C. Koon, C. M. Williams, Q. Zhang, M. Abe, and J. Kirkland, Appl. Phys. Lett. **68**, 2082 (1996).
[12] V. G. Harris, D. J. Fatemi, C. M. Williams, V. M. Browning, J. P. Kirkland, M. X. Chen, S. K. Malik, W. B. Yelon, and G. N. Kryukova, J. Magn. Soc. Jpn. **22**, Suppl. S1, 157 (1998).
[13] D. J. Fatemi, V. G. Harris, V. M. Browning, and J. P. Kirkland, J. Appl. Phys. **83**, 6867 (1998).
[14] D. J. Fatemi, V. G. Harris, M. X. Chen, S. K. Malik, W. B. Yelon, G. J. Long, and A. Mohan, J. Appl. Phys. **85**, 5172 (1999).
[15] E. E. Carpenter, C. J. O'Connor, and V. G. Harris, J. Appl. Phys. **85**, 5175 (1999).
[16] B. Jeyadevan, K. Tohji, K. Nakatsuka, and A. Narayanasamy, J. Magn. Magn. Mater. **217**, 99 (2000).
[17] Adriana S. Albuquerque, Jose D. Ardisson, Waldemar A. A. Macedo, and Maria C. M. Alves, J. Appl. Phys. **87**, 4352 (2000).
[18] V. G. Harris, in *Ferrites: Proceedings of the Eighth International Conference on Ferrites (ICF8), Kvoto, Japan, 2000*, edited by Mansanori Abe and Yohtaro Yamazaki (Japan Society of Powder and Powder Metallurgy, 2000), p. 593.
[19] S. A. Oliver, V. G. Harris, H. H. Hamdeh, and J. C. Ho, Appl. Phys. Lett. **76**, 2761 (2000).
[20] B. Ravel, E. Cockayne, M. Newville, and K. M. Rabe, Phys. Rev. B **60**, 14 632 (1999).
[21] S. D. Kelly, K. M. Kemner, G. E. Fryxell, J. Lie, S. V. Mattigod, and K. F. Ferris, J. Phys. Chem. B **105**, 6337 (2001).
[22] C. J. O'Connor, Candace T. Seip, Everett E. Carpenter, Sichu Li, and Vijay T. John, Nanostruct. Mater. **12**, 65 (1999).
[23] R. A. Neiser, J. P. Kirkland, W. T. Elam, and S. Sampath, Nucl. Instrum. Methods Phys. Res. A **266**, 220 (1988).
[24] K. V. Klementev, J. Phys. D **34**, 209 (2001).
[25] M. Newville, P. Livins, Y. Yacoby, J. J. Rehr, and E. A. Stern, Phys. Rev. B **47**, 14 126 (1993).
[26] W. H. McMaster, N. K. Del Grande, J. H. Mallett, and J. H. Hubbell, Lawrence Livermore Laboratory Report No. UCRL-50174, 1969 (unpublished).
[27] J. J. Rehr and R. C. Albers, Rev. Mod. Phys. **72**, 621 (2000).
[28] A. L. Ankudinov, B. Ravel, J. J. Rehr, and S. D. Conradson, Phys. Rev. B **58**, 7565 (1998).
[29] V. U. König and G. Chol, J. Appl. Crystallogr. **1**, 124 (1968).
[30] S. Calvin, Ph.D. thesis, City University of New York, 2001.
[31] H. J. Krappe and H. H. Rossner, Phys. Rev. B **61**, 6596 (2000).
[32] M. G. Newville, Ph.D. thesis, University of Washington, 1995.
[33] R. D. Shannon, Acta Crystallogr., Sect. A: Cryst. Phys., Diffr., Theor. Gen. Crystallogr. **32**, 751 (1976).